

Experimental energy-loss function, $\text{Im}[-1/\epsilon(q, \omega)]$, for aluminum

P. E. Batson* and J. Silcox

*School of Applied and Engineering Physics, Cornell University, Ithaca, New York, 14853
and The Materials Science Center, Cornell University, Ithaca, New York 14853*

(Received 23 July 1982; revised manuscript received 9 February 1983)

We describe highly accurate (0.2–1%) intensity measurements for the inelastic scattering of 75-keV electrons in $\sim 1000\text{-\AA}$ -thick polycrystalline aluminum films in the region of $(0.0\text{--}3.1)\text{-\AA}^{-1}$ transferred wave vector and $(0\text{--}100)\text{-eV}$ energy loss. The work was performed on the Cornell University electron spectrometer-microscope-computer system. These measurements clarify some experimental problems associated with multiple scattering which obscure the single scattering distribution. We present a new method for eliminating the distribution of intensity attributable to multiple scattering involving quasielastic events. This subtraction method is accurate to $\sim 0.01\%$ of the single-bulk-plasmon intensity. Next, we extend an earlier correction method to obtain the single scattering energy-loss function $\text{Im}(-1/\epsilon)$ from the residue of the first process, which consists of multiple plasmons and quasiparticle transitions. Details of the specific procedures are included. We point out several features in the result—the bulk-plasmon intensity, dispersion, and width, the quasiparticle continuum, and a simultaneous two-plasmon scattering. The latter is, for the first time, characterized completely as to intensity, dispersion, and energy width. Finally, we present a comparison of the measured bulk-plasmon dispersion with some recent model calculations.

I. INTRODUCTION

There has been considerable interest recently in the exploration of low-energy excitations (0–100 eV) in free-electron-like metals^{1–3} and in silicon^{4,5} with both electron energy loss and inelastic x-ray scattering.^{6,7} In this energy region, predominant processes include valence interband transitions,⁸ plasmons,^{9,10} and surface plasmons.^{10,11} Of these, the plasmons and interband transitions have been modeled reasonably successfully by several workers.^{12–14} These models have not included electron exchange and correlation interactions, however, and so there has been further work^{15–17} to include these effects. The experimental investigations mentioned above^{1–5} were conducted in order to determine the magnitude of these interactions to guide the theoretical effort.

We describe here in detail the methods and results of experimental electron-energy-loss measurements on aluminum which have been previously briefly communicated.^{18–20} The work extends earlier efforts^{1–3} and points out problems associated with multiple electron scattering which obscure the desired single scattering energy-loss structure of the materials. It also provides accurate methods for correction of these effects and reveals energy-loss features which have not been observed before.

As described,²⁰ the basic feature bearing on the

strength of the electron-electron interaction is the dispersion $\omega(q)$ of the bulk plasmon, where we use ω as the energy in eV and q as the wave vector in \AA^{-1} . Also, the width $\gamma(q)$ of the plasmon indicates the strength of the collective coupling to other processes, most notably the single-quasiparticle excitations. It is therefore desirable to obtain these parameters,

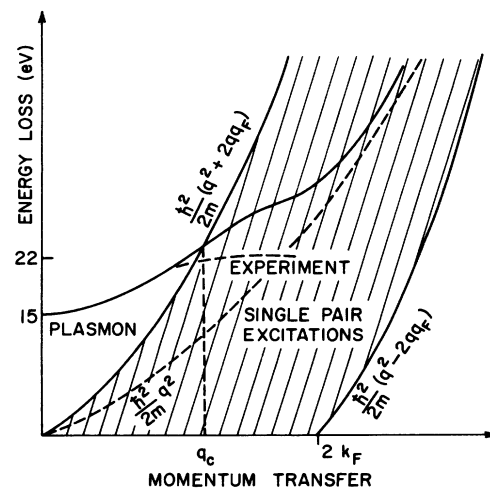


FIG. 1. Low-energy scattering region for electrons in aluminum, showing the bulk-plasmon and the quasiparticle (single pair) excitations. For Al, $q_c = 1.3 \text{ \AA}^{-1}$ and $k_F = 1.75 \text{ \AA}^{-1}$.

found from the intensity $I(q,\omega)$ of the scattered electrons (see, for instance, Raether¹⁰ for a description of electron-energy-loss scattering).

In Fig. 1 we show diagrammatically the expected behavior of $I(q,\omega)$, together with the results of experiments previous to the present work.¹⁻³ The behavior reasonably expected may be predicted from a random-phase-approximation (RPA) calculation¹²⁻¹⁷ and in this figure is shown only schematically. The main result, found both in theory and experiment, is that a collective bulk-plasmon excitation is found rising (for aluminum) from $\omega_p = 15$ eV to $\omega(q_c) = 22$ eV near the critical wave vector $q_c = 1.3 \text{ \AA}^{-1}$ where the plasmon dispersion enters the quasiparticle excitation region. This area extends over a region encompassing $2q_F$ about the classical kinetic energy of the valence electrons. Within this region the behavior of the plasmon appears to be different for the theoretical and the experimental results. Briefly, the dispersion should depart slowly from the small- q form, quadratic with q , according to the strength of interactions of the plasmon with the quasiparticle states. The experimental results suggest a clear underestimation of these effects by the theory.

With the use of an electron microscope equipped with an electron-energy-loss spectrometer,²¹ the authors obtained by photographic means, the scattered intensity as a function of energy loss and scattering angle. The resulting photograph, for a polycrystalline Al film, is shown in Fig. 2(a). Evident in this figure are plasmon losses at 15, 30, and 45 eV, quasielastic losses at 0 eV, quasiparticle losses visible up to the plasmon energy, and many combinations of the above. At 22 eV, the point at which upward dispersion stops in the previous experiments, a horizontal line has been added to the photograph. The bulk plasmon clearly continues through this line to higher energies. Why then did the previous experiments not show this result? The answer is evident in Fig. 3, and has been discussed in detail.¹⁸⁻²⁰ This figure is a contour-map representation of the scattered-intensity data, as a function of energy loss on the vertical axis and scattering angle on the horizontal axis, for $32 \times 256 = 8192$ separate measurements. Clearly evident are the multiple bulk plasmons (*AA, BB, CC, DD, EE*), quasielastic scattering (*FF*), surface plasmons (*G*), and multiple losses involving plasmons and quasielastic events (*II, JJ, KK*), surface plasmons and quasielastic events (*HH*), and finally plasmons, quasielastic events, and surface plasmons (*LL, MM*). The results for the previous electron-energy-loss experiments may be understood by following the peak intensity of the bulk plasmon (*AA*) outward in scattering angle. At $q = 1.8 \text{ \AA}^{-1}$, this intensity is comparable to the in-

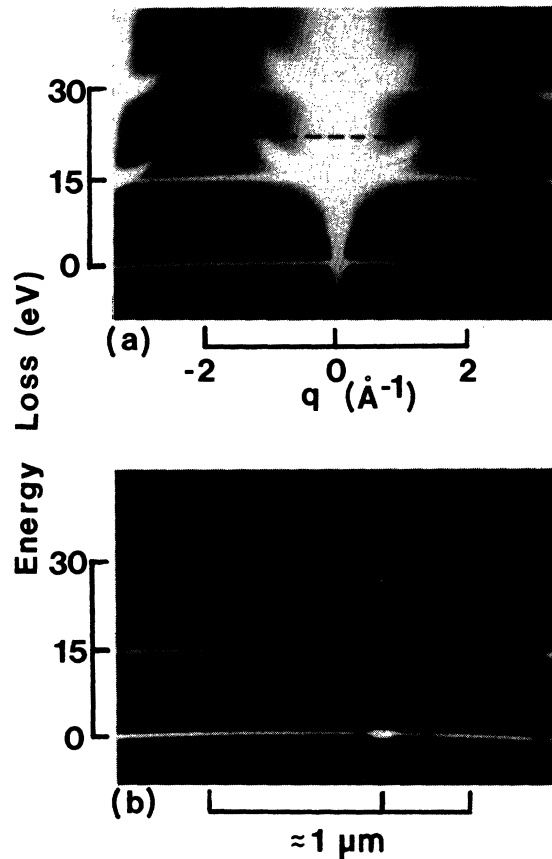


FIG. 2. (a) Photographic intensity as a function of energy loss and scattering momentum transfer (or angle). The dotted line at 22 eV shows the previously obtained asymptotic plasmon dispersion. (b) Photographic intensity as a function of energy loss and image position. The marker indicates a crack in the sample.

tensity of the peak *LL*. Following the maximum in intensity (as a function of energy loss) to larger angles moves the dispersion along the *LL* peak rather than along the plasmon peak. Therefore, a flat dispersion, comparable to the experimental curve in Fig. 1, results when the true dispersion is actually something quite different.

It is apparent, therefore, that measurements of this type require an accurate multiple-scattering treatment. The treatment used was briefly outlined earlier.²⁰ In Sec. II of this paper we present a detailed formulation of the scattering problem and discuss the approximations necessary to arrive at a manageable procedure. The extent of the required accuracy is not realized in general. The presence of the loss *LL* adds about 1% to the intensity present $\omega = 22$ eV and $q = 1.8 \text{ \AA}^{-1}$. Therefore, both the measurements and the correction procedures have to be accurate to 0.1–0.2%. We outline in Sec. III key aspects of an experimental apparatus capable of col-

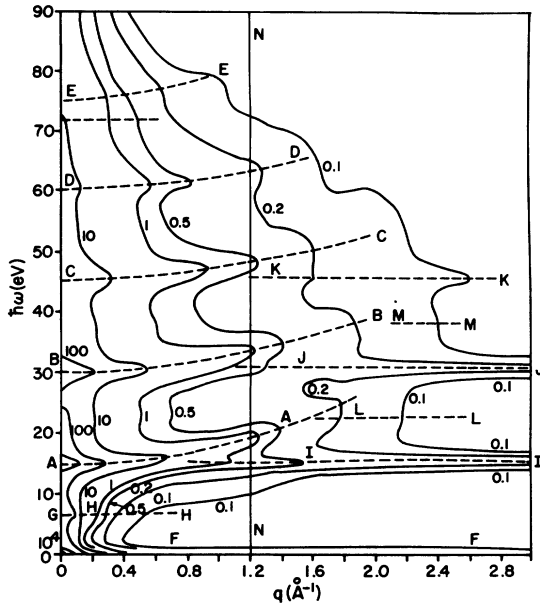


FIG. 3. Intensity contour map for the 910-Å specimen. Note the extreme range of intensity (10^5). The line NN denotes the path covered in energy-momentum space to generate the second spectrum in Fig. 6. The map was generated by combining 32 such scans from 0–100 eV.

lecting data with these accuracies and describe the specific experiment performed to obtain the results in Fig. 3. We then continue in Sec. IV with a description of the specific procedures by which multiple-scattering effects were removed to obtain the “electronic” single scattering function $E_s(q, \omega)$ from the data, where

$$E_s(q, \omega) = \frac{1}{2\pi^2 a_0 E_0} \frac{1}{q^2 + q_E^2} \text{Im} \left[-\frac{1}{\epsilon(q, \omega)} \right], \quad (1)$$

$$q_E = k_0 \frac{\omega}{2E_0},$$

ϵ is the dielectric constant for the material, k_0 is the incident electron momentum, E_0 is the incident electron energy, and a_0 is the Bohr radius. This procedure consists of two parts. The first is a method to remove multiple scattering at large wave vectors which include quasielastic events (the losses FF , HH , II , LL , JJ , MM , and KK in Fig. 3). We believe this is the first suggestion of this method. The second involves a three-dimensional application of a method developed by Misell and Jones^{22,23} of deriving the single scattering from the resulting “electronic” scattering (the losses GG , AA , BB , CC , DD , and EE) using Fourier transforms as suggested by Johnson and Spence.²⁴ Finally, we will point out some features of the resulting distribution that have

not been observed before, and present comparisons with recent calculations.

II. MULTIPLE-SCATTERING CONSIDERATIONS

We begin by defining a scattering distribution $\Sigma_s(\vec{q}, \omega)$ such that

$$\int \Sigma_s(\vec{q}, \omega) d^2q d\omega = \Sigma_T$$

with

$$\Sigma_s = n \frac{d^3\sigma_c}{d\omega d^2q} = \Sigma_T \frac{d^3P}{d\omega d^2q} = \frac{d^3(1/\Lambda)}{d\omega d^2q}.$$

Here σ_c is a conventional cross section, n is the density of scattering centers, $P(\vec{q}, \omega)$ is the scattering probability, Λ is a differential mean free path, and $\Lambda_T = \Sigma_T^{-1}$ is the mean free path due to all excitations in the sample. We divide the sample into slices Δz thick and compute the scattered intensity $I(z + \Delta z, \vec{q}, \omega)$ in terms of $I(z, \vec{q}, \omega)$ using

$$\begin{aligned} \frac{dI(z, \vec{q}, \omega)}{dz} &= -I(z, \vec{q}, \omega) \Sigma_T \\ &+ \int I(z, \vec{q}', \omega') \\ &\times \Sigma_s(\vec{q} - \vec{q}', \omega - \omega') d\omega' d^2q'. \end{aligned} \quad (2)$$

The first term on the right represents the intensity scattered away from the state (\vec{q}, ω) , and the second term—the multiple-scattering term—represents the intensity scattered into (\vec{q}, ω) from a state (\vec{q}', ω') . Since the second term is a convolution integral, Eq. (2) can be solved in Fourier space, giving eventually²³ at the bottom of a slab of thickness t ,

$$\hat{I}(t, \hat{\omega}, \hat{q}) = \hat{I}_0(\hat{q}, \hat{\omega}) e^{-t \Sigma_T} e^{t \hat{\Sigma}_s(\hat{q}, \hat{\omega})}, \quad (3)$$

where the carets denote Fourier transform and the transform variable. If we note that $\hat{I}_0(\hat{q}, \hat{\omega}) e^{-t \Sigma_T}$ is the Fourier transform of the unscattered beam at the bottom of the sample, then in principle $\Sigma_s(\vec{q}, \omega)$ can be obtained from measurements of $I(t, \vec{q}, \omega)$. Practical difficulties exist, however. To successfully invert Eq. (3) all intensity should go smoothly to zero near the transform limits. For purely electronic scattering this can be readily achieved with a film of reasonable thickness but severe problems are encountered with large-angle quasielastic scattering. Since the quasielastic scattering will also be coupled with forward scattered electronic scattering then problems also arise at moderate energy loss. We explore this problem and outline a solution.

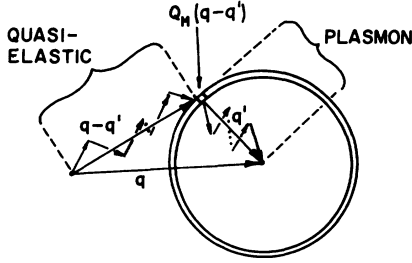


FIG. 4. Geometric construction showing the composition of quasielastic plus plasmon scattering at the point \vec{q} . The multiple scattering is broken up into terms involving only multiple quasielastic scattering and multiple plasmon scattering. The total intensity at \vec{q} is obtained by an integration over all \vec{q}' .

In Fig. 3 we have shown a contour map of the electron intensity scattered from a 910-Å-thick foil specimen as a function of energy loss ω and scattering momentum transfer q . As noted above, the multiple quasielastic plus electronic scattering shows up most strongly in the lines running parallel to the \vec{q} axis at 15.3 eV (*II*), 30.6 eV (*JJ*), etc., which represent bulk-plasmon scattering associated with wide-angle quasielastic scattering. At scattering angles corresponding to a momentum transfer $\sim 1.3 \text{ \AA}^{-1}$ this multiple scattering becomes the dominant feature in the intensity map. To a first approximation, such scattering can be described by the convolution integral

$$\int Q_M(\vec{q} - \vec{q}') E_M(\vec{q}', \omega) d^2 q' ,$$

where $Q_M(\vec{q} - \vec{q}')$ is the wide-angle multiple quasielastic scattering associated with small energy loss (less than the instrumental broadening) of wave vector $\vec{q} - \vec{q}'$, and $E_M(\vec{q}', \omega)$ is the multiple electronic scattering as indicated in Fig. 4. Experimentally, $Q_M(\vec{q} - \vec{q}')$ is slowly varying over much of the area of interest and may be approximated by $Q_M(q)$. Then the convolution integral becomes

$$\{ Q_M(\vec{q}) \delta(\omega) * [\delta(\vec{q}, \omega) + E_M(\vec{q}, \omega)] \}_{\vec{q} = \vec{q}_0}$$

$$= \int Q_M(\vec{q}_0 - \vec{q}') \delta(\vec{q}') d^2 q' \delta(\omega) + \int [Q_M(\vec{q}_0) + Q_M'(\vec{q}_0) |\vec{q}_0 - \vec{q}'| + Q_M''(\vec{q}_0) (\vec{q}_0 - \vec{q}')^2 + \dots] E_M(\vec{q}', \omega) d^2 q' \quad (6)$$

$$= Q_M(\vec{q}_0) \delta(\omega) + Q_M(\vec{q}_0) \int E_M(\vec{q}', \omega) d^2 q' + Q_M''(\vec{q}_0) \int (\vec{q}_0 - \vec{q}')^2 E(\vec{q}', \omega) d^2 q' + \dots , \quad (7)$$

where we have used the fact that E_M is a symmetric in q for our polycrystalline specimen in going from (6) to (7) to eliminate the term linear in q . We finally obtain the form for quasielastically aided multiple scattering at a particular wave vector \vec{q}_0 :

$$\{ Q_M(\vec{q}, \omega) [\delta(\vec{q}, \omega) + E_M(\vec{q}, \omega)] \}_{\vec{q} = \vec{q}_0} = Q_M(\vec{q}_0) \left[\delta(\omega) + \int E_M(\vec{q}, \omega) d^2 q \right] + \dots , \quad (8)$$

where the ellipsis represents terms in even moments of E_M . This verifies the assertion above that these convo-

$$Q_M(q) \int E_M(\vec{q}', \omega) d^2 q' .$$

We verify this form in the following manner. We first notice that the multiple-scattering structure in Eq. (3) can be written

$$e^{i\hat{\Sigma}_s} = 1 + i\hat{\Sigma}_s + \frac{1}{2} i^2 \hat{\Sigma}_s^2 + \dots = 1 + \hat{\Sigma}_M , \quad (4)$$

where Σ_M includes all contributions to the scattering, but excludes the unscattered beam. Σ_M in this case is, of course, thickness dependent. We can break up Σ_M into the corresponding electronic multiple-scattering E_M and quasielastic multiple-scattering Q_M by inserting $\Sigma_s = E_s + Q_s$ into Eq. (4),

$$e^{i\hat{\Sigma}_s} = e^{i\hat{E}_s} e^{i\hat{Q}_s} = e^{i\hat{E}_s} + (e^{i\hat{Q}_s} - 1) e^{i\hat{E}_s} ,$$

so that

$$1 + \hat{\Sigma}_M = (1 + \hat{E}_M) + \hat{Q}_M (1 + \hat{E}_M) ,$$

or, in real space,

$$\delta(\vec{q}, \omega) + \Sigma_M(\vec{q}, \omega) = [\delta(\vec{q}, \omega) + E_M(\vec{q}, \omega) + Q_M(\vec{q}, \omega) * [\delta(\vec{q}, \omega) + E_M(\vec{q}, \omega)] , \quad (5)$$

where the asterisk denotes a convolution integral. The first term of this result includes only the multiple electronic scattering terms, which go smoothly at zero at large scattering angles; the second term contains a mixture of electronic and quasielastic terms, which do not. If this term can be evaluated, a simple subtraction indicated by Eq. (5) cleanly separates the two types of scattering. We continue with some approximations for this term.

We first note that the quasielastic scattering involves energy losses much smaller than our instrumental resolution. Therefore, we approximate $Q_M(\vec{q}, \omega)$ by $Q_M(\vec{q}) \delta(\omega)$. Second, we use the fact mentioned above that $Q_M(\vec{q})$ varies slowly with angle. We therefore expand $Q_M(\vec{q})$ in a Taylor series about some \vec{q}_0 . The last term in Eq. (5) becomes

lution terms are approximated to first order by an integral of the electronic scattering over all angles, weighted by the multiple quasielastic scattering intensity occurring at the particular scattering angle of the measurement.

We have made a number of attempts to estimate $\int E_M(\vec{q}, \omega) d^2q$ from theoretical expressions for $\epsilon(\vec{q}, \omega)$ but none of these has proven to be adequate, and therefore an experimental approach, embodying the characteristics of our particular specimens, is greatly desired. An energy-loss spectrum of an electron-microscope image of our specimen meets these requirements. In Fig. 5, we show an electron ray diagram representing the formation of an image²⁵ of the specimen. It can be seen that the intensity in the image plane represents $\int I(\vec{r}, \Omega) d\Omega$, i.e., the intensity as a function of position integrated over scattering angle, and therefore represents

$$\int [\delta(\vec{q}, \omega) + \Sigma_M(\vec{q}, \omega)] d^2q .$$

This intensity may be related to Eq. (8) by evaluating

$$\int [\delta(\vec{q}, \omega) + \Sigma_M(\vec{q}, \omega)] d^2q = \int [\delta(\vec{q}, \omega) + E_M(\vec{q}, \omega)] * [\delta(\vec{q}, \omega) + Q_M(\vec{q}, \omega)] d^2q . \quad (9)$$

The right-hand side may be expanded into four terms, and evaluated using the assumption that $Q_M(\vec{q}, \omega) \simeq Q_M(\vec{q})\delta(\omega)$, as above. We find

$$\begin{aligned} \int [\delta(\vec{q}, \omega) + \Sigma_M(\vec{q}, \omega)] d^2q &= \delta(\omega) + Q_T\delta(\omega) + \int E_M(\vec{q}, \omega) d^2q + \int E_M(\vec{q}', \omega) Q_M(\vec{q} - \vec{q}') d^2q' d^2q \\ &= (1 + Q_T) \left[\delta(\omega) + \int E_M(\vec{q}, \omega) d^2q \right] , \end{aligned} \quad (10)$$

where $Q_T = \int Q_M(\vec{q}) d^2q$ is the total scattering cross section for quasielastic events. The fourth term has been evaluated by reversing the order of the convolution over q' and the integration over q . Then the prime is dropped. The right-hand side of Eq. (10) is identical to that of Eq. (8) except for the small higher-order terms. Therefore, a simple normalization of the image spectrum, obtained experimentally as in Fig. 6, to the quasielastic intensity at each \vec{q}_0 ,

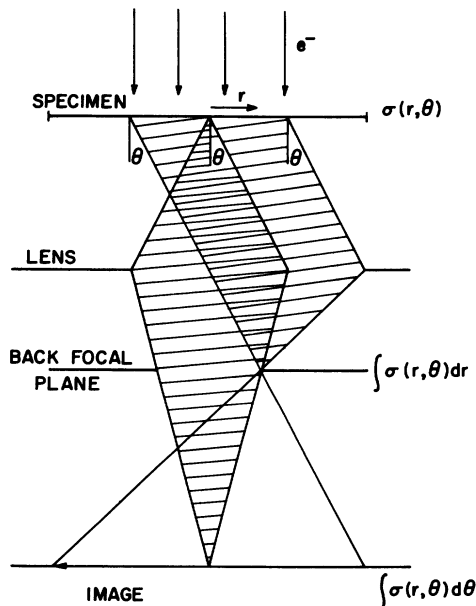


FIG. 5. Electron ray diagram for the electron microscope, showing that intensity in the image is an integration over scattering angle of the intensity scattered by the sample.

produces an intensity distribution which is a very good approximation to the quasielastic plus electronic scattering at \vec{q}_0 . An extremely advantageous feature of this method is that no fitting procedures are required in the region of interest (i.e., near 22 eV in our case). It should be noted that we normally obtain intensity as a function of scattering angle by using the intensity in the back focal plane (shown in Fig. 5), which represents the diffraction pattern and is given by $\int I(\vec{r}, \theta) d^2r$. Therefore, the function $E_M(\vec{q}, \omega)$ in Eq. (8) is clearly integrated over both q and r . If the instrument is operated at low magnification, the effective upper limit of integration over r is determined by the physical size of the spectrometer entrance aperture. Also, even though large angles ($\sim 10^{-2}$ – 10^{-1} rad) are involved this ensures that effects on the image spectrum due to spherical aberration in the microscope lens of Fig. 5 are minor.²⁵ This procedure defines the scattering function $\int E_M(\vec{q}, \omega) d^2q$ for multiple-scattering correction without resorting to guesses or iterative techniques. In Fig. 2(b) we show a photograph of the spectrum obtained from an image of the same specimen used for Fig. 2(a). The resemblance of Fig. 2(b) to the features identified as multiple-scattering features of Figs. 2(a) and 3 are visually striking.

The ideas given above allow the elimination of the large-angle scattering via subtraction of the integrated energy-loss intensity. The residue then diminishes smoothly to zero at large energy loss and scattering angle, allowing use of the Misell-Jones formulation to finally derive the single scattering distribution. These two procedures form the backbone of our single scattering analysis. It now ap-

appears appropriate to comment on the role played by the Fourier-transform procedures. First we note that use of Fourier transforms is dictated by Eq. (3). However, instrumental resolution factors also become important in measurements such as these, which extend over several instrumental runs. Both energy and angular resolution problems have become prominent in our experiments, not so much reflecting intrinsic widths, but day-to-day shape fluctuations as well. Such variations are readily compensated for by using Fourier-transform techniques to deconvolute the variable instrumental shape and to reconvolute a standard shape to avoid development of high-frequency noise. These procedures lead to a considerable improvement in multiple-scattering subtraction techniques, since spectra clearly depend not only on the intensity of the instrumental function but also on its shape. Our procedures in these respects are shown later in Eq. (11) and are described in more detail in the explanation accompanying that equation.

III. EXPERIMENTAL DETAILS

With the comments given above immediately in mind, we outline here the experimental features. The specimen was condensed at a rate of 10–50 Å/sec onto (100) NaCl at room temperature using electron-beam-evaporated 99.999%-pure Al. A background pressure of 5×10^{-8} mm Hg was used and thicknesses were measured with a quartz-crystal thickness monitor. These procedures produce a polycrystalline Al film with a (111) preferred orientation. Earlier work was carried out on polycrystalline films.^{1–3,6} Further, the extensive data acquisition and processing can be reduced considerably because the resulting intensity is a function only of $q = (q_x^2 + q_y^2)^{1/2}$ rather than of q_x and q_y independently, as with single crystals. For a (111) preferred orientation the first significant Bragg ring is the (220) at 4.4 \AA^{-1} . Since we wish to record data out to $\sim 3 \text{ \AA}^{-1}$, elimination of the (111) and (200) rings at 2.6 and 3.1 \AA^{-1} , respectively, is valuable. No cracks were visible in the sample and the grain size was on the order of 200–500 Å. Finally, since we scan out to 100 eV, the thickness should ensure that the scattered intensity at 100 eV should be small enough to minimize truncation errors in the Fourier transform. Thicknesses less than 1500 Å are observed to satisfy this condition. We note that the signal-to-noise ratio deteriorates rapidly for thicknesses less than 200 Å although multiple scattering is still appreciable. Since we therefore have to deal with multiple scattering, the thicker films offer improvement in the signal-to-noise ratio. The films were floated off the NaCl onto distilled

water, picked up on copper grids, and transferred into the microscope in a few hours.

The Cornell University instrument—a Hitachi HU-11A electron microscope and a Wien-filter spectrometer—and the mode of operation have been described elsewhere.²¹ Briefly, 75-keV electrons are focused into a (2–5)- μm -wide spot on the specimen. The angular divergence is $\simeq (1–3) \times 10^{-4}$ rad, giving an angular resolution of approximately 0.11 \AA^{-1} . The energy resolution is limited by thermal effects at the filament and is $\simeq 0.4–1.8$ eV depending on the operating temperature. For our earlier experiments, a regular tungsten filament was used, but we also used a LaB₆ filament²⁶ for some experiments. The latter filament gives a higher intensity with a smaller energy spread and thus eases the time limitations on counting.²⁷

The microscope can be regarded for present purposes as a flexible electron optical bench. Either an image or a diffraction pattern can be recorded photographically or transferred to the plane of the spectrometer entrance slit. The spectrometer then focuses an image of this slit onto a lower screen and disperses the electrons perpendicular to the slit as a function of energy loss. Thus if the slit is selecting scattering angles in a diffraction pattern, then the spectrometer will give intensity as a function of energy loss and scattering angle. This spectrum can be photographed and this mode gives the photographs presented in Figures 2(a) and 2(b). For precise data, however, this is inadequate and it becomes necessary to resort to electron counting. A brief description of our arrangements has been published elsewhere.²⁸

The detection system is built around a minicomputer which controls the spectrometer and records the data. Specifically controlled on line are three devices: the electron spectrometer, x - y deflection coils, and the electron counter. Since, in the diffraction or scattering mode (as opposed to the image mode) the scattered electron intensity is a function of energy loss and of q_x, q_y , the x and y components of the wave vector \vec{q} , then the on-line control enables the computer to set a counting window at a chosen value of ΔE , q_x , and q_y . Information is passed to the spectrometer circuits situated at high voltage by using GaAs light-emitting diodes (LED's) coupled by 15 cm of fiber-optics light pipe to diode light detectors. The speed of the system is such that a position in energy-momentum space can be defined in $\simeq 270 \mu\text{sec}$, allowing count times as small as 1 msec. Therefore, real time observation of data acquisition is convenient. Direct consequences of this capability are as follows. It becomes possible to compensate for long-term fluctuations in beam intensity by sweeping the spectrometer quickly and accumulating many scans. A full scan from 0 to 100 eV

would take between 0.5 and 2.5 sec depending on settings corresponding to 256 points stepped at 0.4 V with counting times varying between 2 and 10 msec. The number of scans chosen depended on intensity—at larger scattering angles ~ 2000 scans were taken corresponding to about 45 min integration. During such lengthy periods, beam alignment also drifts on the order of 10^{-4} rad (0.02 \AA^{-1})—enough to disturb the angular relationship of the scans. Accordingly, the computer periodically scanned in angle across the inelastic beam at 23 eV to determine the maximum, i.e., the incident beam direction, and fed back a compensating deflection to the x - y deflection coils to compensate for such drifts. Instrumental vacuum in the specimen chamber was kept $\sim 10^{-5}$ mm Hg and a liquid- N_2 anticontamination device was used. Nevertheless, contamination became visible in the spectra after ~ 10 min. Accordingly, every 3–4 minutes the scan was halted and a new sample area was brought into view. Finally, it proved necessary to focus the electron beam on the sample by observing the shape of computer-controlled angular scans as a monitor. Reproducibility of the angular divergence, and so the angular averaging of scattered intensity, depended on the most sensitive range of the second condenser lens control and could not be achieved by visual inspection of the final screen alone.

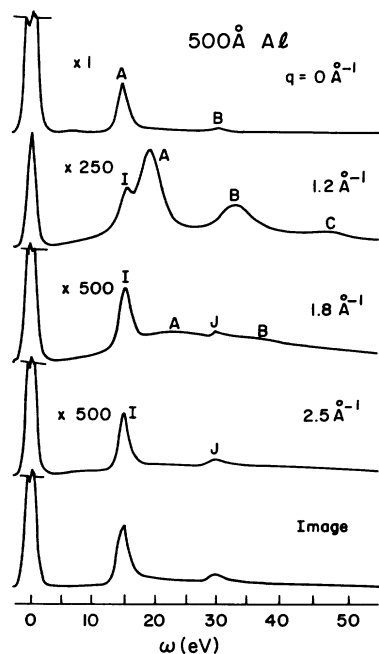


FIG. 6. Energy-loss scans for selected scattering angles and for the image. Notice the dispersion of the bulk plasmon at 15–20 eV, the dominance of multiple scattering above 1.8 \AA^{-1} , and the resemblance of this scattering to the image scan.

The counting system included a plastic scintillator coupled via fiber optics to an EMI-9502S photomultiplier. A 100-MHz programmable counter detected and counted pulses for times of 1–128 msec and data was then transferred from the counter to the computer. This system is capable of linear response over more than 7 orders of magnitude. We note also that the energy calibration over 0–100 V is good to ± 12 meV, i.e., to 10^{-7} . Angular calibrations were achieved by using Bragg reflections.

A number of specimens were studied during the course of this work. However, a complete study was carried out on only two specimens: one of 500-\AA thickness with a tungsten-filament electron source of a full width at half maximum (FWHM) of 1.8 eV, and a specimen of 910-\AA thickness using LaB_6 filament of 0.9 eV FWHM. Our other data are consistent with these specimens and we will focus on these two. The basic experiment consisted of recording 32 energy scans at intervals of 0.1 \AA^{-1} between 0- and 3.1-\AA^{-1} scattering vector. Each scan was composed of 256 points, 0.4 eV apart between 0 and 100 eV. In addition, scans of the image (the integrated cross section) of each specimen were recorded. In Fig. 6 we show a selected series of these scans. These data compare, of course, to that recorded photographically in Fig. 2(a), and a typical path for a scan is identified in Fig. 3. Thus, the scans in Fig. 6 show bulk plasmons A , B , and C as the prominent features at low angles. As the scattering angle approaches 1.2 \AA^{-1} we see the development of multiple quasielastic plasmon scattering I, J which by 1.8 \AA^{-1} has clearly become the dominant term in the scattering. The similarity of the image spectrum to that at 2.5 \AA^{-1} is also evident. These scans were then used to produce the contour map shown in Fig. 3, of measured intensity as a function of ω and q . It is perhaps worthwhile emphasizing that, for the most part, the accuracy of the intensity measurements reported here surpasses the ability of the draftsman and printer to reproduce them on plots of this nature.

Our concern has been predominantly with the region $1.4\text{--}2.2 \text{ \AA}^{-1}$ and the energy region between 20 and 30 eV, where the question concerns the existence of peaks A and LL (Fig. 3) and their appropriate identification. We have already published intensity scans in momentum-transfer (\vec{q}) (or angle) at constant energy^{18,20} providing evidence for continuation of peak A up to 28 eV, and a precise (0.2% statistics) energy scan at 1.8 \AA^{-1} showing evidence of two peaks at 22.4 and 24.7 eV.²⁰ We reproduce the latter figure here as Fig. 7 for the sake of continuity in the development of our argument. These two peaks are reflected also in the 0.2 contour at $q = 1.8 \text{ \AA}^{-1}$ in Fig. 3, corresponding to the development of LL

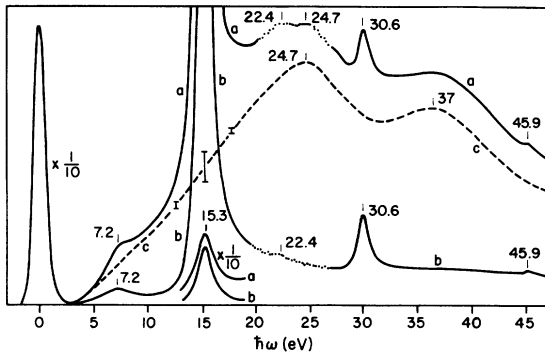


FIG. 7. Scan *a* at 1.8 \AA^{-1} showing the existence of two peaks between 20 and 30 eV. The lower peak is a multiple-scattering event and is exactly reproduced in the image scan *b*. The difference between the two, scan *c*, shows only the upper peak (after Batson, Chen, and Silcox, Ref. 20.)

away from *A*. Figure 7 clearly shows the existence of these two peaks and the reason (the need for 0.2% statistical accuracy) that they have not been observed before.

To generate Fig. 3 we have found it necessary, as mentioned above, to compensate for day-to-day fluctuations in the instrumental conditions. We therefore deconvolute from the data the incident energy spectrum and reconvolute a standard (Gaussian form) analogous to the method used in Eq. (11) below. In addition, normalization is necessary in the angular axis. This was accomplished primarily by fitting each energy-loss scan intensity to an angular scan at either zero energy or at the plasmon energy, whichever intensity is larger.

IV. ANALYSIS OF EXPERIMENTAL DATA

First, we wish to eliminate the $L_{2,3}$ core excitation loss at 72 eV. Accordingly, an exponentially decaying tail (matched in intensity and slope at 65 eV) replaces the measured intensity above 65 eV. Although the most probable shape²⁹ for this tail is actually the power law $\Delta E^{-4.5}$, we found the exponential form slightly more convenient. Since the total intensity in this region was about 0.1% of that at the plasmon intensity, the exact shape was not important for this work.

A. Quasielastic multiple scattering

We now come to the problem of removing the multiple quasielastic electronic scattering. As discussed in detail earlier the approach is to use an image spectrum suitably normalized to the quasielastic peak at $\omega=0$ eV as an approximation to the quasielastically aided multiple scattering. In Fig. 8,

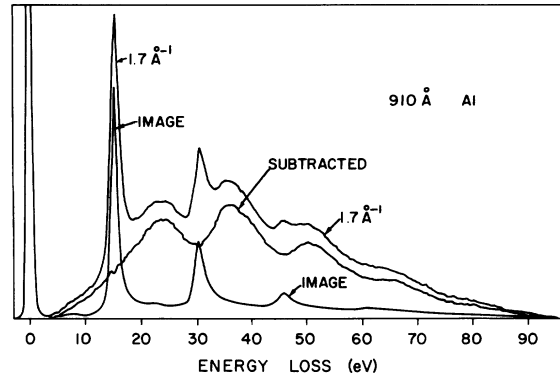


FIG. 8. Subtraction of the image spectrum from the spectrum at 1.7 \AA^{-1} . This result emphasizes that, although 0.2% statistics are required to see the two peaks in Fig. 7, this accuracy is not required to perform satisfactory correction if only gross features are desired.

we show two such spectra, an energy scan taken at 1.7 \AA^{-1} and an image scan with the $\omega=0$ peaks normalized as outlined below. We note that the peaks in the image spectrum occur precisely at peak points of the multiple-scattering peaks. For example, the first quasielastic peak occurs at 15.3 eV in both the scans rather than at 14.9 eV as is observed in a $q=0$ scan. Similarly, the intensity ratio in the

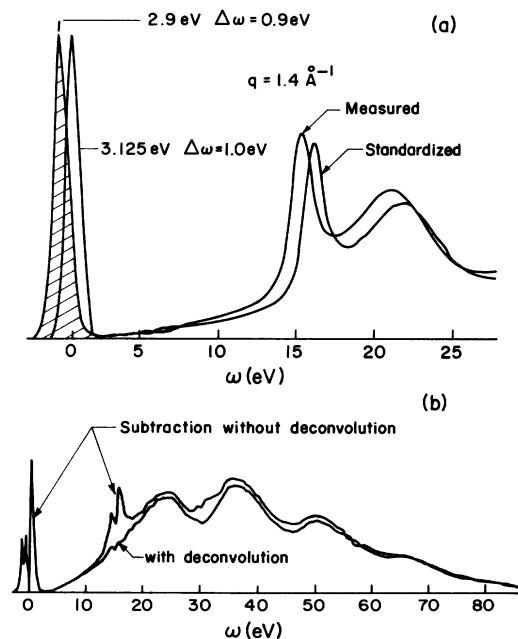


FIG. 9. (a) Replacement of an instrumental resolution of uncertain shape with a Gaussian of standard width and position. Note that although the Gaussian has a higher FWHM, it encompasses less intensity, leading to smaller scattered peaks. (b) Comparison of an image subtraction with and without resolution standardization.

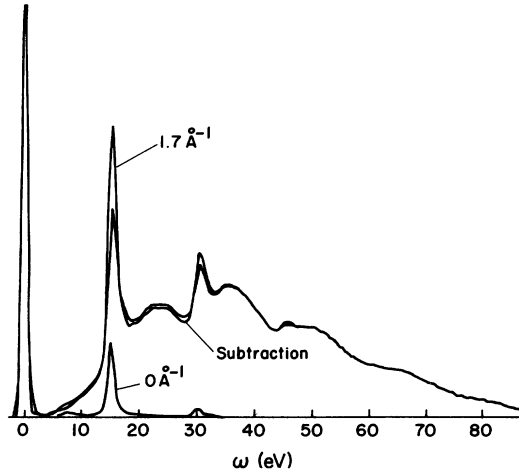


FIG. 10. Subtraction carried out using the $q = 0 \text{ \AA}^{-1}$ scan rather than the image scan. The result here is clearly inadequate because the instrumental angular resolution is much smaller than q_E . This may not have been the case in Ref. 1 where it has been used.

peaks is correct, as is evident in the subtracted spectrum also shown in Fig. 8. To be specific, if we let $Q_M(\vec{q}_0, \omega)$ and $Z_I(\omega)$ be the energy distribution of the peak at $\omega = 0$ (defined to cover the region $-1.0 \text{ eV} < \Delta E < 2.0 \text{ eV}$), for the energy scan at q_0 and the image scan, respectively, and if $I_M(\vec{q}_0, \omega)$ and $I_I(\omega)$ are the complete intensity distributions, then the subtracted, normalized scan involving only elastic and electronic scattering (I_E) is given in Fourier space (ω only) as

$$\begin{aligned} \hat{I}_E(q_0, \hat{\omega}) &= \hat{G}(\hat{\omega}) \exp[t\hat{E}_s(q_0, \hat{\omega})] \\ &= \hat{G}(\hat{\omega}) \left[\frac{\hat{I}_M(q_0, \hat{\omega})}{\hat{Q}_M(q_0, \hat{\omega})} - \frac{\hat{I}_I(\hat{\omega})}{\hat{Z}_I(\hat{\omega})} \right], \quad (11) \end{aligned}$$

where $\hat{G}(\hat{\omega})$ is the Fourier transform of a standard instrumental resolution. In this case $G(\omega)$ is chosen to be a Gaussian at a position of 3.125 eV and FWHM of 1 eV. In Figs. 9 and 10 we illustrate the need for these procedures. Thus in Fig. 9(a) we show the result of replacing the instrumental resolution, in a measured intensity scan, with the standard Gaussian. It should be noted that not only do peak positions shift but also changes in peak heights occur reflecting changes in incident beam width and, therefore, total incident intensity. In this example, in fact, a Gaussian of broader width than the instrument actually encompassed less intensity, leading to smaller peaks. In Fig. 9(b) we show the effect of attempting the image subtraction without compensating for changes in the incident beam energy shape. Residual intensity spikes at the strong multiple-scattering plasma peaks are clearly evident. Finally,

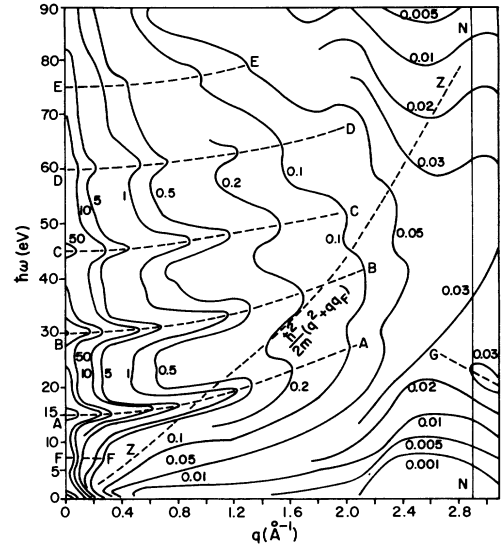


FIG. 11. Intensity contour map after application of the image subtraction. Note the enhancement of the Bragg plus plasmon scattering (GG).

in Fig. 10, we show an example of the use of a $q = 0$ scan as the quasielastically aided scattering term.¹ The inadequacies of this procedure are clearly evident in the residual quasielastic-plasmon peaks left at 15, 30, and 45 eV, even though the quasielastic peak at 0 eV has been completely removed. Comparing this result with Fig. 8, it should now be evident that the use of relationship (11), i.e., taking account of quasielastic electronic multiple scattering using image scans and appropriate normalization procedures, is necessary to achieve a satisfactory stripping of the quasielastic electronic scattering. Finally, Fig. 7 shows in more detail the achievable accuracy of this method. We emphasize that what is involved is the fitting of the image spectrum with the scan at q only in the immediate vicinity of $\omega = 0$ eV. Once this is done, no further approximations need be considered. We therefore have the ideal situation wherein no fitting procedures are required in the region of our desired intensity measurements. The amount of multiple-scattering corrections at energy losses greater than 2 eV are not adjusted, after the initial normalization at zero energy, as they are in iterative techniques.

B. Bragg multiple scattering

In Fig. 11 we show the intensity contour map resulting from the calculations of Eq. (11). Several features have been made more visible by this process. First, it can be seen that the losses HH , II , JJ , KK , etc. have been cleanly removed. In addition, the loss LL at 22 eV and $1.8\text{--}3.0 \text{ \AA}^{-1}$ is absent,

leaving the bulk plasmon (AA) much more prominent. As highlighted by the dotted line (ZZ), the edge of the quasiparticle continuum is beginning to appear. Finally, the Bragg plus plasmon scattering (GG) appears for $q > 2.2 \text{ \AA}^{-1}$. This intensity must be eliminated before the processing may be continued. The expected intensity for this scattering is estimated from

$$I_{\text{Bragg}} + I_{\text{pl}}(\vec{q}, \omega) = \int I_{\text{Bragg}}(\vec{q} - \vec{q}') I_{\text{pl}}(\vec{q}', \omega) d^2 q', \quad (12)$$

where the integration can be cut off at q values less than that at which this correction becomes necessary. Therefore, the result of Fig. 11 is used for $I_{\text{pl}}(\vec{q}', \omega)$ and I_{Bragg} is experimentally measured.

After this correction, we have a result including only the valence electron, or “electronic,” scattering. This falls off nicely at large energy loss and scattering angles. We note in passing that a numerical integration over angle of either these data, or the original raw data, matches the aperture investigation of the image distribution closely, thus justifying the derivation of Eq. (10). (Indeed, the draftsman was unable to reproduce the differences; so we eliminate an illustration).

C. Single scattering

The multiple-scattering corrections are continued by implementing the Misell-Jones method for deriving the single scattering electronic distribution. We invert Eq. (11) and find for E_s

$$\hat{G}(\hat{q}, \hat{\omega}) t \hat{E}_s(\hat{q}, \hat{\omega}) = \hat{G}(\hat{q}, \hat{\omega}) \ln \frac{\hat{I}_E(\hat{q}, \hat{\omega})}{\hat{G}(\hat{q}, \hat{\omega})}. \quad (13)$$

Here $G(\hat{q}, \omega)$ is identified with $I_0(\hat{q}, \omega) e^{-t \Sigma_r}$ and is the standardized unscattered beam determined as a function of \vec{q} by Eq. (11), when those results are combined to form Fig. 11. Here, as in Eq. (11), $G(\vec{q}, \omega)$ is used also to control noise in the resulting spectra. Notice that the specimen thickness does not appear as a parameter of the calculation. In this single scattering derivation, it appears only in the absolute magnitude of the single scattering function, not in its shape. We finally may obtain an average, $\langle E_s(\vec{q}, \omega) \rangle$, by dividing Eq. (13) by the total volume under $tG(\vec{q}, \omega)$ to give the differential inverse mean free path for “electronic” scattering. We note here a computational difficulty. First, the above Fourier transforms are strictly three dimensional in character (ω, q_x, q_y with $q_z \simeq 0$ through conservation of

momentum). As pointed out above, we have reduced the required number of measurements by using a polycrystalline sample with rotational symmetry about $q = 0$. The two-dimensional Fourier transform for q_x and q_y may therefore be replaced by the one-dimensional Fourier-Bessel transform (FBT).³⁰

We therefore compute Eq. (13) using a fast Fourier transform³¹ for the ω variable and a FBT for the q variable. Secondly, as is evident in Fig. 11, the scattered intensity varies 7 orders of magnitude over the range of measurements. Transform techniques with 24-bit floating-point accuracy experience truncation errors for even 10% accuracy if this dynamic range is not reduced. Equation (1) indicates, however, that a large part of this variation is merely the term $1/(q^2 + q_E^2)$. We may approximate this term with an exponential e^{-aq^2} , which has a well-defined FBT ($e^{-p\hat{q}^2}$).³⁰ We therefore subtract this exponential form, Fourier-Bessel transform the residue, and add the appropriate exponential transform to the result.

D. Obtaining the energy-loss function

Finally, we wish to obtain the energy-loss function $\text{Im}[-1/\epsilon(q, \omega)]$. Here we must also include some practical considerations. In this experiment the instrumental resolution $G(\vec{q}, \omega)$ has a width larger than $2q_E$. Therefore, the measured value of $E_s(\vec{q}, \omega)$ is blurred. This blurring can be evaluated approximately by averaging over an effective aperture:

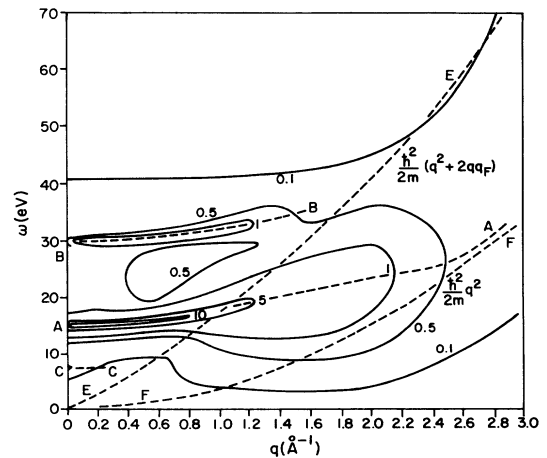


FIG. 12. $\text{Im}[-1/\epsilon]$ for the 910-Å sample. Notice the bulk plasmon (AA), the quasiparticle edge (EE), the two-plasmon event (BB), and the surface plasmon (CC).

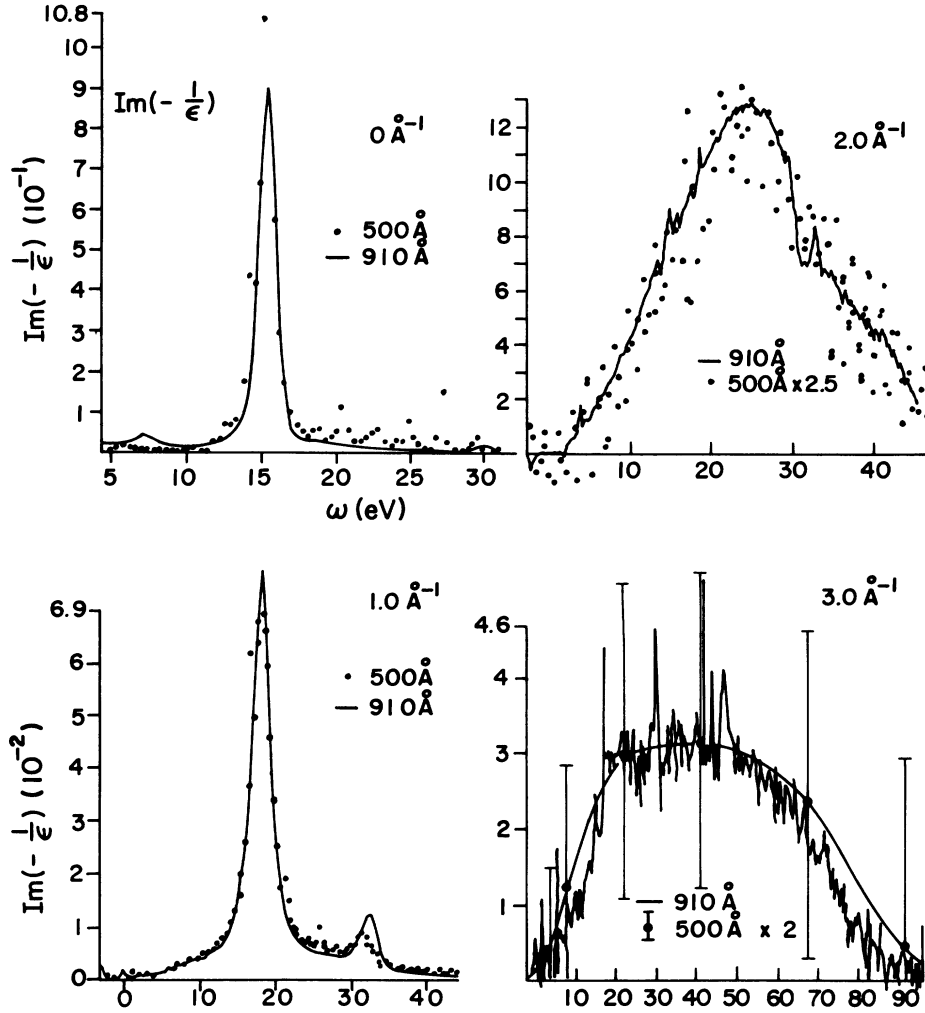


FIG. 13. Comparison of $\text{Im}(-1/\epsilon)$ for the two samples. Note the statistical improvement with the 910-Å sample.

$$\begin{aligned}
 \langle E_s(q, \omega) \rangle &\approx \frac{1}{2\pi^2 a_0 E_0} \text{Im} \left[-\frac{1}{\epsilon} \right] \frac{1}{\pi (\Delta q_R)^2} \int_0^{2\pi} d\phi \int_0^{\Delta q_R} \frac{\Delta q d\Delta q}{q^2 + q_E^2 + (\Delta q)^2 - 2q \Delta q \cos\phi} \\
 &\approx \frac{1}{2\pi^2 a_0 E_0} \text{Im} \left[-\frac{1}{\epsilon} \right] \frac{1}{(\Delta q_R)^2} \ln \left[1 + \frac{(\Delta q_R)^2}{q^2 + q_E^2} \right], \quad (14)
 \end{aligned}$$

where $2\Delta q_R$ is the width of the resolution function $G(\vec{q}, \omega)$. This result has a significantly different shape from Eq. (1). We therefore invert Eq. (14) and use the result to calculate $\text{Im}(-1/\epsilon)$. This result containing the structure intrinsic to the sample composition is shown in Fig. 12.

E. Consistency checks

A comparison of the results for the 500- and 910-Å samples shows $\sim 15\%$ agreement in the absolute intensity at most measurement points. Above 2.0 \AA^{-1} , they are different by about a factor of 2. This

difference appears to be consistent with the statistical accuracy of the measurements at these wave vectors, i.e., above 2.0 \AA^{-1} the resulting, corrected intensity is $\sim 1\%$ of the measured intensity at the same point while we have obtained measurement accuracies of 0.2–1%. Examples of spectra at different scattering angles are shown in Fig. 13. The only significant shape difference lies in the statistical accuracy of the two. Significantly better results were obtained from the 910-Å sample both because the higher-brightness electron LaB₆ source was used and because a thicker sample provides more scatter-

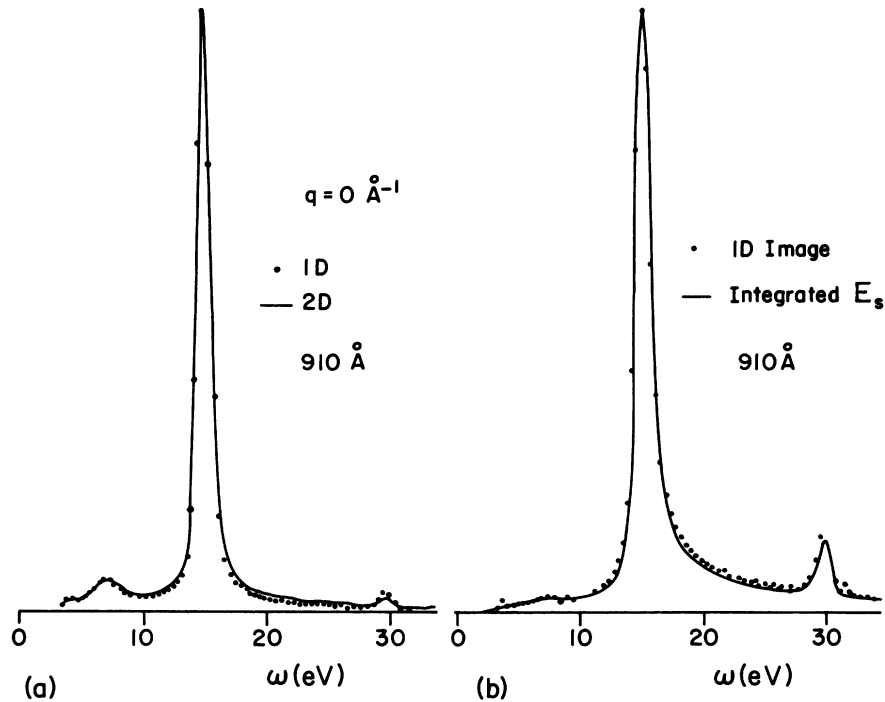


FIG. 14. (a) Comparison of the one-dimensional single scattering derivation for $q=0 \text{ \AA}^{-1}$, with the $q=0 \text{ \AA}^{-1}$ result from $E_s(q,\omega)$. (b) Comparison of the one-dimensional single scattering result for the image spectrum, with the integral over q of $E_s(q,\omega)$.

ing, and, hence, more information with which to perform the above analysis.

The apparent intensity dip at $q=0$ in Fig. 12 probably reflects inaccuracies in Eq. (14). However, an intensity deficiency of about 6% for the 910-Å sample is also expected at small wave vector ($\sim q=0.006 \text{ \AA}^{-1}$) due to a surface correction at the bulk-plasmon frequency as pointed out by Ritchie.³² This deficiency is also expected to be thickness dependent, becoming about 10% for the 500-Å sample. Therefore, care must be exercised when comparing results from specimens of different thickness.

In Fig. 14 we show checks of the three-dimensional multiple-scattering treatment. We noted above that the previous work utilizing the Misell-Jones formulation was done for the ω variable only.^{24,33} We show two examples of similar work with the aluminum. First, in Fig. 14(a) we show the result of an ω variable analysis for the $q=0 \text{ \AA}^{-1}$ raw spectrum and compare it to the $q=0 \text{ \AA}^{-1}$ trace from the complete result for $E_s(\vec{q},\omega)$. We expect these results to be comparable since the scattering is largely in the forward direction. Next, in Fig. 14(b) we compare the ω variable analysis of the raw image spectrum, with the numerical integration over all angles of $E_s(\vec{q},\omega)$. Agreement in both cases is remarkable. These checks

serve to verify that the numerical procedures followed to evaluate Eqs. (11), (13), and (14) did, in fact, closely approximate the analytical forms required.

V. RESULTS OF THE ANALYSIS

A. Characterization of the plasmon

We first point out in Fig. 12 the presence of the bulk-plasmon AA beginning at $\omega=14.95 \text{ eV}$ and $q=0 \text{ \AA}^{-1}$ and dispersing upwards at roughly constant intensity to about 18 eV and 0.9 \AA^{-1} . At this point its intensity decreases rapidly due to interaction of the plasmon with the quasiparticle continuum. We therefore assign this value of 0.9 \AA^{-1} to q_c in agreement with the results of Gibbons *et al.*³ We may determine a total mean free path for the plasmon alone by evaluating

$$\Lambda^{-1} = \int_{-10}^{20} \int_0^{q_c} E_s(\vec{q},\omega) q dq d\omega . \quad (15)$$

We find $\Lambda=1370 \text{ \AA}$ for the 500-Å sample and 1210 Å for the 900-Å sample. The evaluation for a simple free-electron-gas dielectric constant with q dependence was shown by Raether¹⁰ to be

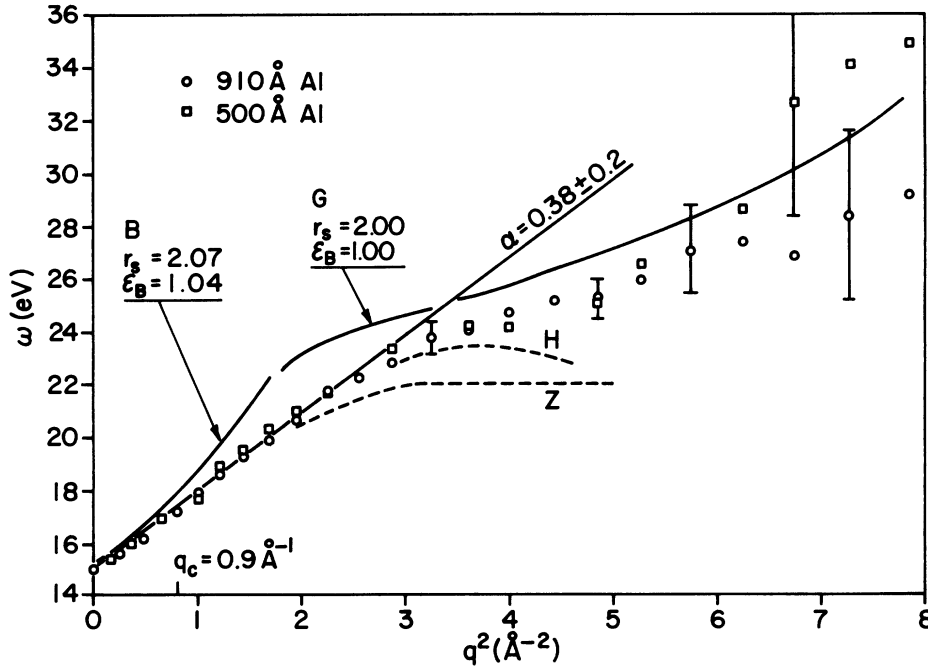


FIG. 15 Bulk-plasmon dispersion $\omega(q)$. The previous results are from Ref. 1 (A) and Ref. 2 (H). α is defined by Eq. (17), and agrees with Refs. 1 and 2. Model results are from Ref. 38 (B) and Ref. 43 (G).

$$\Lambda \approx \frac{2a_0}{\omega_p} E_0 \left[\ln \left(\frac{q_c}{q_E(\omega_p)} \right) \right]^{-1}, \quad (16)$$

where a_0 is the Bohr radius, ω_p is the plasma energy, and E_0 is the incident electron energy (75 keV). This expression produces $\Lambda = 1240 \text{ \AA}$ for $q_c = 0.9 \text{ \AA}^{-1}$, in reasonable agreement. If the experimental mean free path for all angles and energy losses is computed we find $\Lambda = 725$ and 670 \AA for the 500- and 900- \AA samples, respectively. Previous measurements of Λ have obtained 920 \AA (Ref. 34) and $850 \pm 150 \text{ \AA}$ (Ref. 35). It appears likely, therefore, that those measurements, which relied on an empirical fit of multiple-scattering peaks at moderately large energies with Poisson-distributed peak intensities, were affected by scattering into single-particle continuum states which are present under the large energy-loss peaks.

The plasmon dispersion also flattens slightly as it enters the quasiparticle region, and approaches the center of the continuum at $\omega = q^2/2m$. In Fig. 15 we plot the plasmon-peak maximum positions as a function of q^2 together with the results of Zacharias¹ and of Hochberger, Otto, and Petri.² We note a marked difference between the present data and the previous results. As was pointed out in Ref. 20, we believe that this difference is due to the interference of triple scattering involving quasielastic, plasmon, and surface-plasmon scattering which we

have removed. This is emphasized by the observation of the fact that curve H is approximately an intensity-weighted average of the positions of the plasmon and the triple-scattering peaks as shown in Fig. 7. Clearly, the wide variation of peak positions in the experimental results of Zacharias¹ and of Hochberger, Otto, and Petri² emphasizes the difficulty in estimating the multiple-scattering intensity by other than an experimental method.

The plasmon dispersion is linear with q^2 out to about 1.7 \AA^{-1} and

$$\omega = \omega_p + \alpha \frac{\hbar^2}{m} q^2, \quad (17)$$

with $\omega_p = 14.95 \pm 0.05 \text{ eV}$ and $\alpha = 0.38 \pm 0.02$. Other values for ω_p are 15 ,^{3,9} 14.8 ,³⁵ 14.95 ,³⁶ and 14.81 – 15.3 .³⁷ Other values for α are 0.42 ,¹ 0.41 ,³ and 0.5 .⁹ From Fig. 12 it is clear that this quadratic dispersion persists well into the quasiparticle region. Deviation from this does not occur until the strength of $\text{Im}(-1/\epsilon)$ is reduced to 10% of its $q = 0 \text{ \AA}^{-1}$ value. The plasmon is therefore a well-defined bulk oscillation at wave vectors well beyond q_c .

In Fig. 16 we show the large-angle dependence of the width of the plasmon. At small angles we note that the product of the strength and width remains constant until $q_c = 0.9 \text{ \AA}^{-1}$. This is easily seen in Fig. 12 and is in agreement with the theoretical results of Sturm.³⁸ A detailed comparison with this

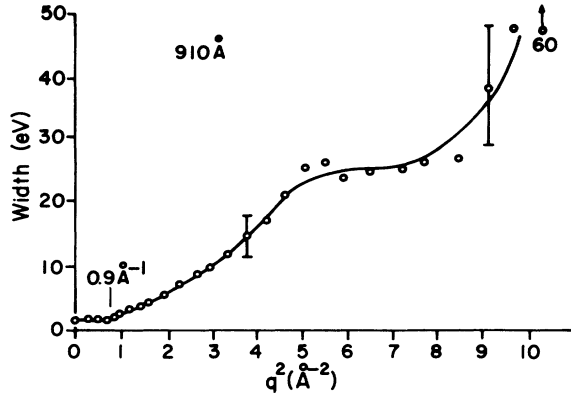


FIG. 16. Bulk-plasmon width, including the 1-eV instrumental broadening.

theory is, however, not possible due to the present instrumental energy-loss resolution of 0.9 and 1.6 eV. We note a smooth increase in the width until $q \approx 2.3 \text{ \AA}^{-1}$, where there is an apparent transition to a width more characteristic of the quasiparticle region. This is noticeable in Fig. 13 where the data at 2.0 \AA^{-1} retains a peaked shape near 25 eV in contrast to the broad distribution present at 3.0 \AA^{-1} .

We therefore generally describe the plasmon as being unaffected by the continuum until about $q_c = 0.9 \text{ \AA}^{-1}$. It retains its dynamic characteristics while being damped until 1.2 \AA^{-1} , at which point it has been reduced to 10% of its original strength. From 1.7 to about 2.3 \AA^{-1} it appears to have become a mixture of collective and single-particle states. Finally, above 2.3 \AA^{-1} there appear to be only single-particle states present.

B. Comparison of plasmon dispersion with theory

The RPA model for the electron gas, as formulated by Lindhard,¹² predicts a value of 15.8 eV for ω_p in Al ($r_s = 2.07$). There are, however, several recent formulations that shift this result toward the observed value of 14.95.

It is clear that in a real metal the periodic nature of the ionic background must be taken into account. This has been done recently by Bross³⁹ where it was shown that interband transitions near 14 eV and higher in Al shift the plasmon energy downward by 0.3 eV. This calculation correctly predicts the observed value of 11.3 eV for the Fermi energy, confirming other similar calculations⁴⁰ and therefore justifying the use of an electron effective mass $m^*/m = 1.025$ (Refs. 39 and 40) to correct approximately for band-structure effects.

Ionic-core to conduction-band transitions also contribute a further downward shift. These are included by calculating a uniform background dielec-

tric constant ϵ_B for $L_{2,3}$ core excitations. This is estimated for Al^{3+} ions in the crystal lattice to be 1.039.⁴¹ Also, we have confirmed this estimate by integrating the experimental $L_{2,3}$ photon absorption intensity⁴² to find the oscillator strength. From this result we find $\epsilon_B = 1.037$. The K-core contribution is found to be negligible.⁴³ This background, when combined with values of $\partial\epsilon/\partial\omega$ obtained from Bross, produces a further shift of 0.27 eV downward.

In Fig. 15 we show the results from Bross including corrections given above for the core excitations. The asymptotic slope at $q = 0$ is in good agreement with the observed slope. The theoretical value for ω_0 of 15.23 eV is, however, too large. At this time there does not appear to be an understanding of this discrepancy.

For $q > q_c$, electron exchange and correlation effects become important. These have been treated by Vashishta and Singwi,¹⁷ who showed that the dispersion coefficient α is lowered from its RPA value of 0.42 to about 0.34. Recently, a modification of this approach by Gupta *et al.*⁴⁴ was shown to be moderately successful in matching the dispersion well above q_c . This result, calculated for $r_s = 2.00$, is reproduced here in Fig. 15. It is significantly different from the data only in the region $q_c < q < 2q_c$, apparently because it does not break away from the Lindhard RPA result at small enough wave vectors.

If the Gupta result is scaled at small wave vector to $r_s = 2.07$, $m^* = 1.025m$, and $\epsilon_B = 1.04$, then we find agreement with the Bross result. It is clear, therefore, that all these processes are necessary to begin to understand the experimental result.

C. Short-range correlations

A large q ($\sim 2.7\text{--}3.0 \text{ \AA}^{-1}$) mode near 23 eV has been reported by Platzman *et al.*⁴⁵ and has been the subject of several recent theoretical papers.^{46,47} We are unable to confirm the presence of this mode, although the present result is not inconsistent with its possible existence. Consideration of Fig. 11 (line GG) points out that, at least for electron scattering, significant peaking occurs near 23 eV and 2.8 \AA^{-1} due to Bragg scattering followed by plasmon scattering as described by Eq. (12). In the present work this term in the multiple scattering was not dealt with at a sufficient level of precision. Care should therefore be exercised in the interpretation of peaks in this region unless it can be shown that multiple scattering is small.

D. Two-plasmon scattering

In Figs. 12–14 there is clearly residual intensity near 30 eV which has not been removed by the

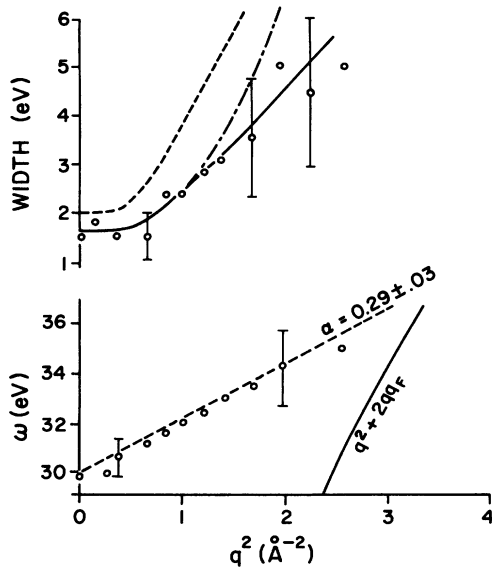


FIG. 17. Dispersion and width for the two-plasmon event. α is defined as in Eq. (17); the dotted line shows the expected behavior for the convolution of two independent plasmons, and the dot-dashed line shows the single-plasmon behavior. The widths here include a 0.9-eV instrumental resolution.

Misell-Jones single scattering derivation. This indicates that there is some incidence of correlated scattering of more than one plasmon. That this result is not a mistake in the processing is confirmed by direct peak-area measurements of raw data, such as those shown in Fig. 6, which show an excess of intensity in the two-plasmon peak above that predicted by Poisson statistics. This excess is consistent with that shown by the processing.

The behavior of this correlated two-plasmon peak is shown in Fig. 17 and is as follows: (a) The dispersion of its energy with wave vector is linear with q^2 and follows Eq. (17) with $\omega_p = 30 \pm 0.8$ eV and $\alpha = 0.29 \pm 0.03$; (b) its width is approximately constant out to 0.9 \AA^{-1} and increases swiftly thereafter in a manner roughly consistent with the width of the single plasmon; (c) the intensity has a minimum near $q=0$ and increases to a maximum near $q=0.2-0.3 \text{ \AA}^{-1}$; (d) the cross section for this process is measured to be about 7% of the cross section for single-plasmon production

These observations most likely agree with the

two-plasmon calculations developed by Ashley and Ritchie⁴⁸ which investigate the possibility of the simultaneous production of two plasmons. The absence of a long-lived bound state with a finite binding energy in this theory is in agreement with the $q=0$ asymptotic energy found to be just twice the single-plasmon energy. Also, the dispersion we have found is in agreement with that expected for the convolution of two independent plasmons.

The measurements of linewidth and intensity, however, suggest a real interaction between the two-plasmon states. As shown in Fig. 17 the two-plasmon width does not agree with the convolution width of two independent plasmons. Also, the depression of intensity near $q=0$ suggests a correlation of the plasmon wave vectors, excluding the association of two plasmons traveling in opposite directions. Alternate explanations may be the failure of Eq. (14), or interference of the negative surface term, as noted above. The Ashley-Ritchie theory may be able to explain these observations because it predicts the formation of a short-lived bound state of two plasmons which immediately breaks up to form two independent plasmons. An investigation of the damping mechanisms for this model is needed to determine if it can explain the present results.

Finally, this model predicts a cross section of between 4 to 10% of the single-plasmon cross section, in agreement with the present result of 7%. We note that previous work by Spence and Spargo³³ on Al and Sn also revealed residual intensity in agreement with this cross-section prediction.

We do not find agreement with the theory of Ruvalds *et al.*⁴⁹ which predicts a finite two-plasmon binding energy and significant deviation from the simple dispersion curve seen in the experiment. We note that recent work by DuBois and Goldman⁵⁰ has shown an error in the Ruvalds work. The correction of this error significantly reduces the prediction of a long-lived coupled mode in a material like Al.

We wish to thank Professor J. Wilkins, Dr. R. H. Ritchie, Dr. C. H. Chen, and P. Garik, for many helpful discussions during the course of this work. Financial support from the National Science Foundation through the Cornell University Materials Science Center is gratefully acknowledged.

*Present address: IBM Thomas J. Watson Research Center, Yorktown Heights, N. Y. 10598.

¹P. Zacharias, *J. Phys. C* **7**, 126 (1974); *J. Phys. F* **5**, 645 (1975).

²H. Hochberger, A. Otto, and E. Petri, *Solid State Commun.* **16**, 175 (1975).

³P. C. Gibbons, S. E. Schnatterly, J. J. Ritsko, and J. R. Fields, *Phys. Rev. B* **13**, 2451 (1976); J. J. Ritsko, S. E. Schnatterly, and P. C. Gibbons, *Phys. Rev. Lett.* **32**, 671 (1974).

⁴J. Stiebling and H. Raether, *Phys. Rev. Lett.* **40**, 1293 (1978).

- ⁵C. H. Chen, A. E. Meixner, and B. M. Kincaid, *Phys. Rev. Lett.* **44**, 937 (1980).
- ⁶D. Miliotis, *Phys. Rev. B* **3**, 701 (1971).
- ⁷N. G. Alexandropoulos, *J. Phys. Soc. J.* **31**, 1790 (1971).
- ⁸E. Petri and A. Otto, *Phys. Rev. Lett.* **34**, 1283 (1975).
- ⁹H. Watanabe, *J. Phys. Soc. J.* **11**, 112 (1956).
- ¹⁰H. Raether, in Vol. 38 of *Springer Tracts in Modern Physics*, edited by G. Höhler (Springer, Berlin, 1965), p. 85.
- ¹¹C. J. Powell and J. B. Swan, *Phys. Rev.* **115**, 869 (1959); **118**, 640 (1960).
- ¹²J. Lindhard, *Dan. Vidensk. Selsk. Mat. Fys. Medd.* **28**, 8 (1954).
- ¹³D. Pines, *Elementary Excitations in Solids* (Benjamin, New York, 1964), p. 138.
- ¹⁴D. Bohm and D. Pines, *Phys. Rev.* **92**, 609 (1953).
- ¹⁵J. Hubbard, *Proc. R. Soc. London, Ser. A* **243**, 336 (1957).
- ¹⁶D. J. W. Geldhart and S. H. Vosko, *Can. J. Phys.* **44**, 2137 (1966).
- ¹⁷P. Vashishta and K. S. Singwi, *Phys. Rev. B* **6**, 875 (1972); **6**, 883 (1972).
- ¹⁸P. E. Batson, C. H. Chen, and J. Silcox, *Bull. Am. Phys. Soc.* **20**, 410 (1975).
- ¹⁹P. E. Batson, C. H. Chen, and J. Silcox, *Bull. Am. Phys. Soc.* **21**, 351 (1976).
- ²⁰P. E. Batson, C. H. Chen, and J. Silcox, *Phys. Rev. Lett.* **37**, 937 (1976).
- ²¹G. H. Curtis and J. Silcox, *Rev. Sci. Instrum.* **42**, 630 (1971).
- ²²D. Misell and A. F. Jones, *J. Phys. A* **2**, 540 (1969).
- ²³T. Grove, *Ultramicroscopy* **1**, 15 (1975).
- ²⁴D. W. Johnson and J. C. H. Spence, *J. Phys. D* **7**, 771 (1974).
- ²⁵P. B. Hirsch, A. Howie, R. B. Nicholson, D. W. Pashley, and M. J. Whelan, *Electron Microscopy of Thin Crystals* (Butterworths, London, 1965).
- ²⁶S. D. Ferris, D. C. Joy, H. J. Leamy, and C. K. Crawford, in *Proceedings of the 8th Scanning Electron Microscopy Symposium 11, Chicago (1975)*, edited by O. Johari and I. Corvin (IITRI, Chicago, 1975).
- ²⁷P. E. Batson, C. H. Chen, and J. Silcox, in *Proceedings of the 34th Electron Microscopy Society of America, Miami (1976)*, edited by G. W. Bailey (Claitors, Baton Rouge, Louisiana, 1976).
- ²⁸P. E. Batson, J. Silcox, and R. Vincent, in *Proceedings of the 29th Electron Microscopy Society of America, Boston (1971)*, edited by C. J. Arceneaux (Claitors, Baton Rouge, 1971), p. 30.
- ²⁹R. F. Egerton, *Philos. Mag.* **31**, 199 (1975).
- ³⁰E. J. Burr, *Aust. J. Phys.* **8**, 30 (1955).
- ³¹J. W. Cooley and J. W. Tukey, *Math. Comput.* **19**, 297 (1965).
- ³²R. H. Ritchie, *Phys. Rev.* **106**, 874 (1957).
- ³³J. C. H. Spence and A. E. C. Spargo, *Phys. Rev. Lett.* **26**, 895 (1971); and in *Proceedings of the 8th International Congress on Electron Microscopy II, 390, Canberra (1974)*, edited by J. V. Sanders and D. J. Goodchild (Australian Academy of Sciences, Canberra, 1974).
- ³⁴R. E. Burge and D. L. Misell, *Philos. Mag.* **18**, 261 (1968).
- ³⁵A. W. Blackstock, R. H. Ritchie, and R. D. Burkhoff, *Phys. Rev.* **100**, 1078 (1955).
- ³⁶R. B. Pettit, R. Vincent, and J. Silcox, *Phys. Rev. B* **11**, 3116 (1975).
- ³⁷T. Kloos, *Z. Phys.* **265**, 225 (1973), and Refs. 10–20 contained therein.
- ³⁸K. Sturm, *Z. Phys.* **28**, 1 (1977); *Z. Phys. B* **25**, 247 (1976).
- ³⁹H. Bross, *J. Phys. F* **8**, 2631 (1978).
- ⁴⁰B. Segall, *Phys. Rev.* **124**, 1797 (1961).
- ⁴¹L. Pauling, *Proc. R. Soc. London, Ser. A* **114**, 181 (1927); C. Kittel, *Introduction to Solid State Physics* (Wiley, New York, 1968), p. 385.
- ⁴²C. J. Powell, *Rev. Mod. Phys.* **48**, 33 (1976).
- ⁴³R. Leapman (private communication).
- ⁴⁴A. K. Gupta, P. K. Aravind, and K. S. Singwi, *Solid State Commun.* **26**, 49 (1978).
- ⁴⁵P. M. Platzman and P. Eisenberger, *Phys. Rev. Lett.* **33**, 152 (1974).
- ⁴⁶G. Mukhopadhyay and A. Sjölander, *Phys. Rev. B* **17**, 3589 (1978).
- ⁴⁷H. DeRaedt and B. DeRaedt, *Phys. Rev. B* **18**, 2039 (1978).
- ⁴⁸J. C. Ashley and R. H. Ritchie, *Phys. Status Solidi* **38**, 425 (1970).
- ⁴⁹J. Ruvalds, A. K. Rajagopal, J. Carbello, and G. Grest, *Phys. Rev. Lett.* **36**, 274 (1976).
- ⁵⁰D. F. DuBois and M. V. Goldman, *Phys. Rev. Lett.* **40**, 257 (1978).

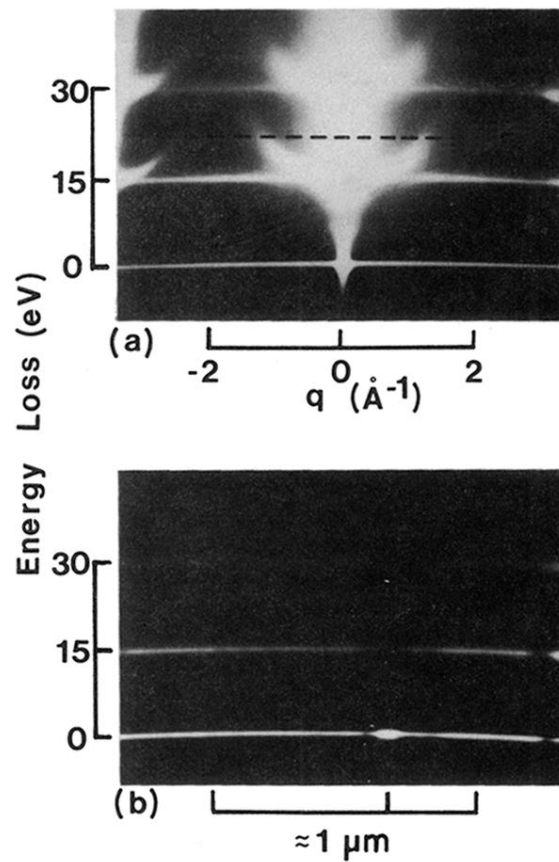


FIG. 2. (a) Photographic intensity as a function of energy loss and scattering momentum transfer (or angle). The dotted line at 22 eV shows the previously obtained asymptotic plasmon dispersion. (b) Photographic intensity as a function of energy loss and image position. The marker indicates a crack in the sample.